metals

MDPI

Article

Casting Simulation-Based Design for Manufacturing Backward-Curved Fan with High Shape Difficulty

Chul Kyu Jin

School of Mechanical Engineering, Kyungnam University, 7 Kyungnamdaehak-ro, Masanhappo-gu, Changwon-si 51767, Republic of Korea; cool3243@kyungnam.ac.kr; Tel.: +82-55-249-2346

Abstract: A large-sized backward-curved fan with high shape difficulty was designed, and fan performance was roughly predicted from computational fluid dynamics. Three gating systems of aluminum sand casting were designed to fabricate the fan. The flow pattern and solidification process of molten metal were analyzed by casting simulation. Three types were applied: bottom-up with four gates, bottom-up with ten gates, and top-down with a feeder. The simulation results of the bottom-up with four gates show that a large temperature loss occurs while molten metal flows into thin blades, and there is a temperature range below the liquidus temperature. Due to nonuniform temperature distribution, the solidification pattern is also not uniform. The bottom-up with ten gates shows almost similar flow and solidification patterns but has the effect of slightly reducing the temperature loss of molten metal. The top-down type has a much smaller temperature loss, while molten metal flows into the mold cavity compared to the bottom-up type and has a directional solidification pattern. As the feeder also acts as a riser to compensate for the shrinkage of the thick part, the simulation results regarding porosities are also significantly reduced. The fan cast as a top-down type has soundness without any unfilled parts.

Keywords: casting simulation; gating system design; sand casting; centrifugal fan; backward fan; blade

check for updates

Academic Editor: Jaime Lazaro-Nebreda

Received: 8 December 2024
Revised: 2 January 2025
Accepted: 14 January 2025
Published: 21 January 2025

Citation: Jin, C.K. Casting Simulation-Based Design for Manufacturing Backward-Curved Fan with High Shape Difficulty. *Metals* **2025**, *15*, 99. https://doi.org/10.3390/met15020099

Copyright: © 2025 by the author. Licensee MDPI, Basel, Switzerland. This article is an open access article distributed under the terms and conditions of the Creative Commons Attribution (CC BY) license (https://creativecommons.org/licenses/by/4.0/).

1. Introduction

A blower is a device that increases the speed of air by rotating blades. The kinetic energy of the blades increases the amount and pressure of air at the outlet. It is classified into fans and blowers depending on the discharge pressure. If the pressure is less than 0.1 kg/cm^2, it is a fan, and if the pressure is 0.1 to 1.0 kg/cm^2, it is a blower. Fans are classified into centrifugal fans and axial fans depending on the direction of air movement and the shape of the blade. Centrifugal fans transport air in the radial direction of the blade, and axial fans transport air in the axial direction by the propeller blade. Centrifugal fans have different characteristics depending on the blade shape and the installation angle of the blades and include multi-blade fans, plate fans, backward-curved fans, and air foil fans. Backward-curved fans belong to turbo fans because their pressure and efficiency are relatively high and they can operate quietly even at high speeds of over 4000 rpm. Axial fans have relatively low pressure and efficiency but have the advantage of blowing a large amount of air [1–7].

The tank uses a water-cooled diesel twin turbo V12 engine. The engine's displacement is 47,000 cc, and the output is 1120 kW at 2600 rpm. The engine is equipped with two centrifugal backward-curved fans. When the engine operates at maximum speed, the fan rotates at an appropriate speed to prevent engine overheating and regulate the engine

temperature. If a sufficient cooling effect is not delivered by the fan when the engine is running, the engine may suffer serious damage. Therefore, to increase the cooling effect, a fan combining the turbo type and the axial type is used in tanks [8].

The general manufacturing method for centrifugal fans is to shape the blades through plastic deformation or machining processes and then assemble them by welding or fastening them to shrouds. Another manufacturing method is sand casting, which produces blades and shrouds as one body [9–12]. Since 2015, research on manufacturing blades using 3D printers has been conducted [13–15]. The shape of the blade of the fan used in a tank is bent in the radial direction and also in the axial direction, so the shape difficulty is quite high. Additionally, it must rotate at a high speed of 2600 rpm. Therefore, considering efficiency, weight, noise, vibration, etc., the sand casting process that can be manufactured as an integrated body is suitable.

The shape of the centrifugal fan is almost similar to the pump impeller. Some research has been conducted on mold design and casting simulation for small pump impeller casting, and there are also studies [14,16–19]. Dermawan and Pramono [20] manufactured the SS316L pump impeller using the investment casting method. Wang et al. [21] and Choe et al. [22] used 3D printing technology for investment casting of impeller. Kuo et al. [23] and Wang et al. [24] performed mold design using numerical simulation for investment casting of the impeller. Ma et al. [25] applied the die-casting method to manufacture a magnesium alloy impeller. Liu et al. [26] manufactured a SUS 304 impeller by applying a low-pressure casting process. Wallace et al. [27] manufactured an aluminum alloy impeller using the thixocasting process. Hafeez et al. [28] applied a new technology called ablation sand casting to manufacture an aluminum alloy impeller. Little research has been conducted on casting mold design and casting simulation for centrifugal backward-curved fans. In particular, there are no studies on large sizes.

In this study, a large-sized aluminum backward-curved fan was designed, and fan performance was roughly predicted from computational fluid dynamics. The gating system of sand casting was conducted for a large-sized fan whose shape is quite complex. Three gating systems were designed, and the optimal gating system was selected using casting simulation software. A large-sized fan with no casting defects was produced through an optimal gating system of sand casting.

2. Design

2.1. Geometry of the Backward-Curved Fan

Figure 1 shows the shape of a backward-curved fan. The overall shape is similar to a closed-type pump impeller with a shroud. The unique feature of the fan is its blade shape, which is a fusion of the centrifugal fan's backward type and axial fan type. The blade is curved in the radial direction and also has a curve in the axial direction. The number of blades is 15. The fan has a front shroud in the direction where air flows in and a back shroud in the direction where it is combined with the engine. The outer diameter of the fan is Ø645 mm, and the height of the hub is 180 mm. The diameter of the inlet through which air flows in is Ø510 mm, and the diameter of the outlet through which air flows out is Ø645 mm. In the casting process, molten metal is filled into a mold cavity made identical to the product shape and then solidified. Therefore, the thickness of a product is a very important design factor in fluidity. The thickness of the shell structure, including the shroud, is more than 15 mm. As can be seen in Section A-A and Section B-B, the cross-sectional thickness of the blade varies depending on the location. The thickness of the part where the blades are connected to the hub is 11.5 to 21.3 mm, and the thickness of the part where the blades are connected to the shroud is 5.5 to 8.0 mm. The cross-sectional thickness of the blade is 5.7 to 7.5 mm, and the thickness of the blade ends of the inlet and

outlet is 5.5 mm. The thinnest part of the fan is the blade end and the part where the blades are connected to the shroud. The minimum thickness is approximately 5.5 mm. Blades are curved in the radial direction and also in the axial direction. Therefore, considering the thickness and shape of the blade, the shape difficulty for sand casting can be said to be quite high. The surface area and volume of the fan are 2,515,655 mm^2 and 9,723,000 mm^3, respectively. The surface area to volume ratio is approximately 2.5. The weight, applying the density of aluminum (2.77 g/cm^3), is 26.93 kg.

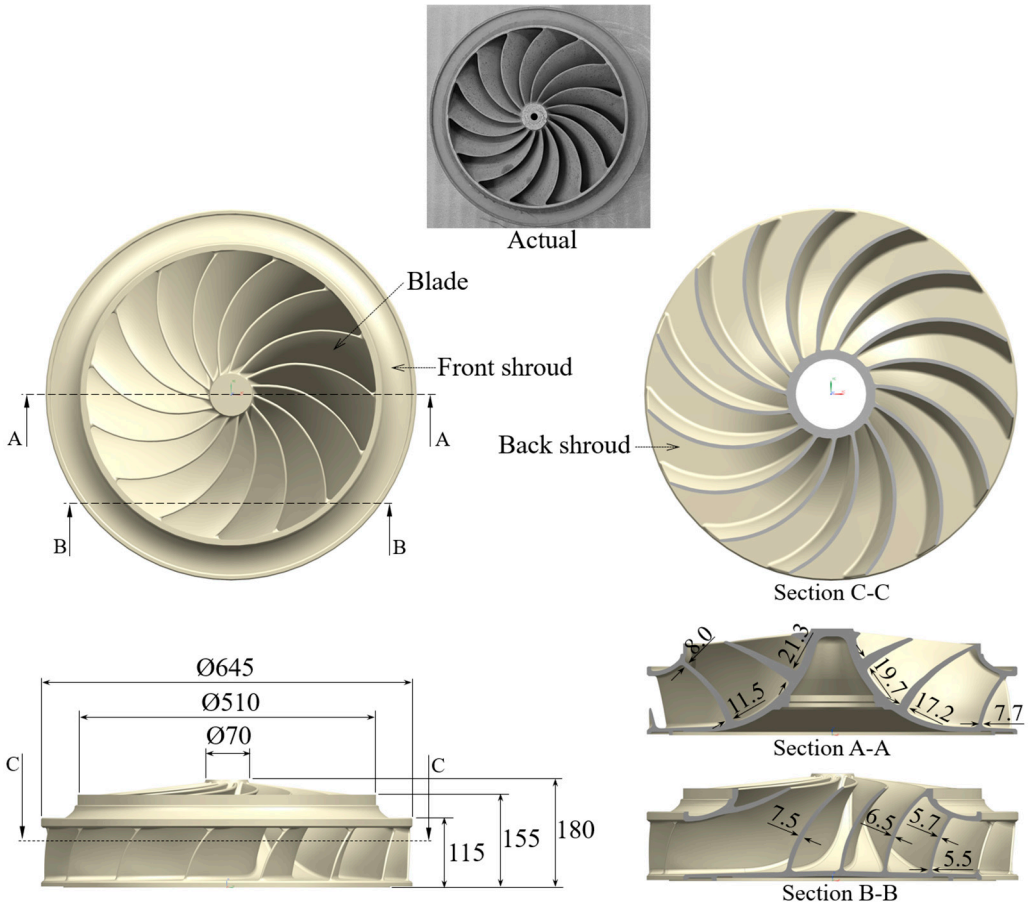

Figure 1. Two-dimensional dimensions of the backward-curved fan.

2.2. Flow Analysis and Structural Analysis of Backward-Curved Fan

Flow analysis used Ansys Fluent, and 3D steady-state analysis was performed. Ansys Static structure was used for structural analysis, and pressure was received from flow analysis for load conditions. The fluid area for flow analysis consists of three areas: inlet area, fan area (frame motion), and housing area. The inlet is the place where air flows in, and the frame motion is the area where the fan rotates and is under the condition of rotating counterclockwise. The outlet of the housing is where the fluid flows out. The incoming fluid was air, the rotation speed of the fan was set to 4600 rpm, and the outdoor air conditions were set to 20 °C and 1 atm. The air flow rate was set to 9.51 m^3/s, and the air density was applied at 1.204 kg/m^3, which is 1 atm. The mass flow rate of air entering the inlet for the set conditions was 11.486 kg/s. Figure 2 shows the simulation results performed with Ansys Fluent. Figure 2a shows the static pressure distribution of the fan. The pressure increases from the inlet to the outlet. The tip of the blade is red and shows high pressure distribution because it collides with the air head-on. The pressure distribution on the back of the blade is relatively low due to counterclockwise rotation. Figure 2b shows the velocity distribution. The air inside the fan has a high speed, and the cross-section at

the outlet is rapidly enlarged, so the velocity decreases. From the flow analysis results, the required power and pressure drop at the inlet and output were calculated. Pressure drop was calculated as the value at the fan's inlet and outlet area surrounding the fan's exterior. Because pressure values are derived differently for each element, static pressure was calculated using an area-weighted average. The fan's inlet is −8242.3 Pa, and the outlet is 432.2 Pa. In other words, the pressure drop from the fan's inlet to the outlet is 8674.5 Pa. The torque acting on the fan is 286.8 N·m, and when multiplied by the rotation speed (4600 rpm), the required power of 138.2 kW is calculated. Pressure drop is a value that excludes most losses or irreversible factors, and power is a value that does not take into account various losses. The static pressure calculated from flow analysis was applied as a load condition for static structural analysis. As a constraint condition, fixed support was applied to the central hole of the fan. Figure 3 shows the total deformation and equivalent stress analysis results. The maximum value of total deformation occurs at the end of the blade of the fan at 0.00078 mm, and the maximum value of equivalent stress occurs at the fillet part at the bottom of the fan blade, which is 0.241 MPa.

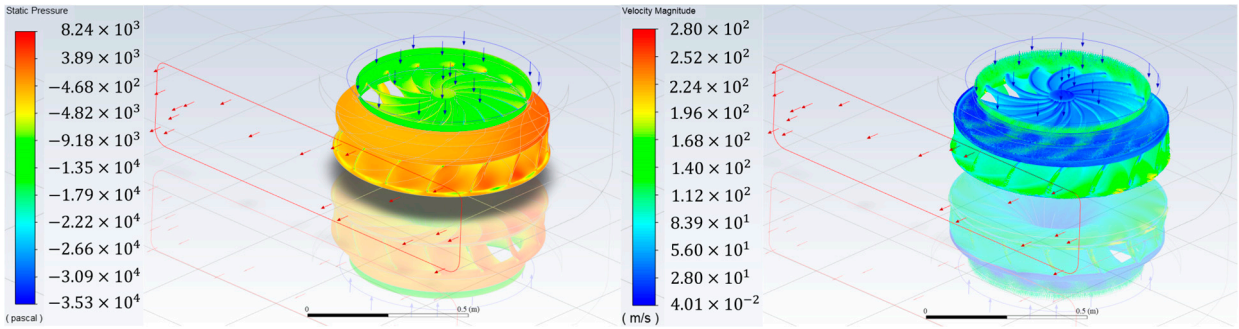

(**a**) (**b**)

Figure 2. Simulation results by Ansys Fluent: (**a**) static pressure; (**b**) velocity.

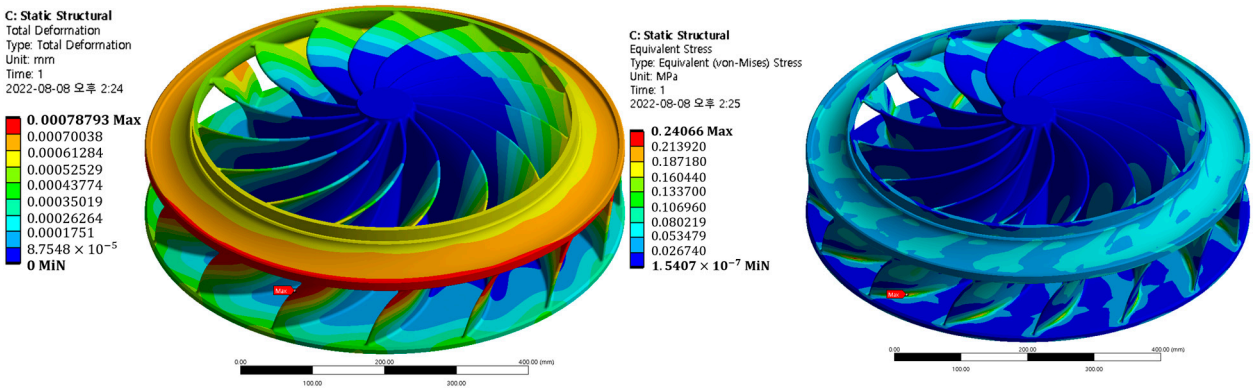

(**a**) (**b**)

Figure 3. Simulation results by Ansys Static structural: (**a**) total deformation; (**b**) equivalent stress.

2.3. Gating System of Sand Casting

In order to manufacture a backward-curved fan with a high degree of difficulty in shape using sand casting, gating system design must be carried out. Before designing the gating system, the plane of division of the casting pattern was first determined. The top mold and bottom mold were divided based on the bottom surface of the fan. The effective height was calculated from the plane of division of the casting pattern, and then the minimum cross-sectional area was calculated. Three gating systems for backward-curved fans were designed, and casting simulation was performed to select the optimal

design. The minimum cross-sectional area was calculated for designing gating systems. The cross-sectional areas of sprue, runner, and gate could be obtained from the minimum cross-sectional area and Sprue:Runner:Gate (S:R:G) ratio [29,30]. Figure 4 shows three gating system designs applied to the backward-curved fan. Figure 4a,b show bottom-up types in which molten metal flows from the bottom side and rises upward. Figure 4c shows a top-down type in which molten metal flows from the top center and moves downward. The gating system in Figure 4a,b is a method in which molten metal is poured into the sprue, passes through the runner, and flows into the fan through each gate. Aluminum has a relatively small specific gravity, so the flow velocity may increase while flowing into the mold cavity, causing turbulence. Therefore, an unpressurized gating system was applied to control the flow velocity of molten metal. The unpressurized gating system is designed to have the largest cross-sectional area of the gate among the sprue, runner, and gate, as well as the smallest cross-sectional area of the sprue.

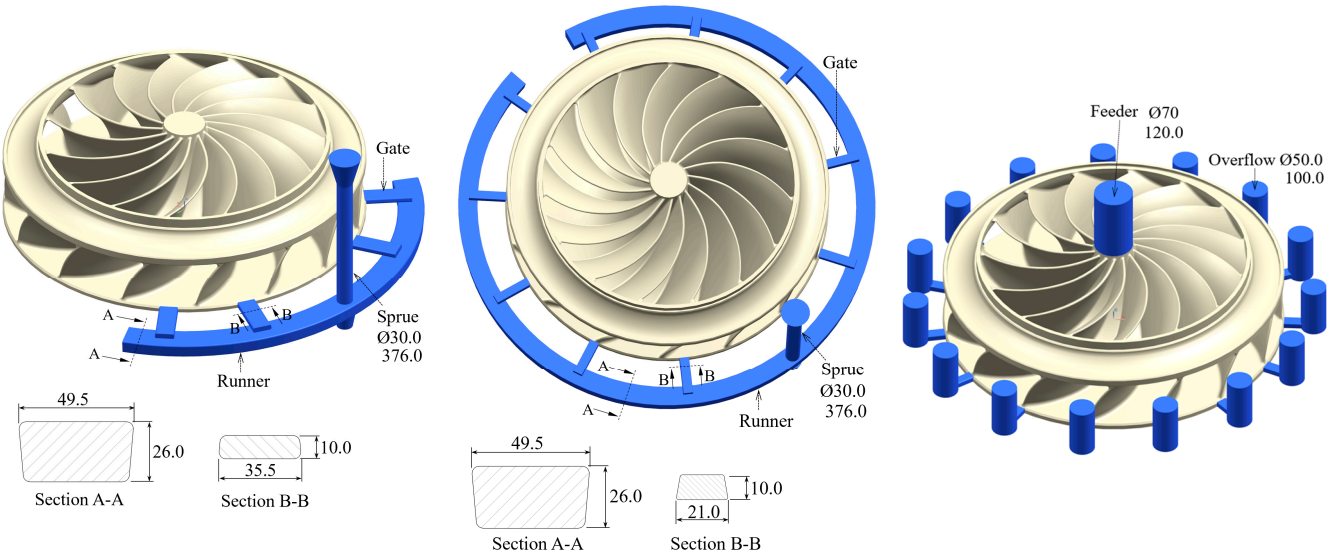

Figure 4. Three types of gating systems for the backward-curved fan: (**a**) bottom-up with four gates; (**b**) bottom-up with ten gates; (**c**) top-down (unit: mm).

The bottom-up gating system in Figure 4a has four gates, and two gates are arranged at 25° intervals on each side of the sprue. The runner surrounds approximately 28% of the fan. The diameter of the sprue is Ø30.0 mm, and the length of the sprue is 376.0 mm. Section A-A is the cross-section of the runner, and Section B-B is the cross-section of the gate. The cross-sectional shape of the runner and gate is trapezoidal. The cross-sectional area of the runner is 1240.2 mm^2. The cross-sectional area of each gate is 353.0 mm^2, and the total cross-sectional area of the four gates is 1412.0 mm^2. The volume and weight of the gating system are 1,477,700 mm^3 and 4.09 kg, respectively. The bottom-up gating system in Figure 4b has ten gates, and five gates are arranged at 33° intervals on both sides of the sprue. The runner surrounds the entire fan. The diameter and length of the sprue and the cross-sectional area of the runner are the same as in Figure 4a. The cross-sectional area of each gate is 192.0 mm^2, and the total cross-sectional area of the ten gates is 1920.0 mm^2. The volume and weight of the gating system are 3,845,200 mm^3 and 10.65 kg, respectively. The SRG ratio of the designed gating system is 1.00:1.75:2.00 in Figure 4a and 1.00:1.75:2.71 in Figure 4b. The recovery rate for the weight of the fan compared to the total weight is 84.6% in Figure 4a and 71.6% in Figure 4b. Figure 4c is a top-down type in which molten metal is poured into the feeder and immediately flows into the fan. Unlike Figure 4a,b,

there are no runners and gates, and there is only a feeder that functions as a sprue. The feeder has a diameter of Ø70 mm, and it is located in the center of the top of the fan. At the bottom of the fan, an overflow was placed on the side of the back shroud to remove the initially introduced molten metal from the fan. The number of overflows is 15, and the diameter and height are Ø50.0 mm and 100 mm, respectively. The volume of the feeder and overflow is 3,678,200 mm^3, and the weight is 10.19 kg. The recovery rate is 72.5%. Table 1 shows data on volume, weight, and recovery rate for three gating systems: bottom-up with four gates, bottom-up with ten gates, and top-down type. Figure 5 shows a sand mold in which the plane of division of the casting pattern was determined based on the bottom surface of the fan.

Table 1. Data of three gating systems for the backward-curved fan.

Gating System Type	Volume (mm^3)	Weight (kg)	Recovery Rate (%)
Bottom-up with four gates	1,477,700	4.093	84.6
Bottom-up with ten gates	3,845,200	10.651	71.6
Top-down	3,678,200	10.189	72.5

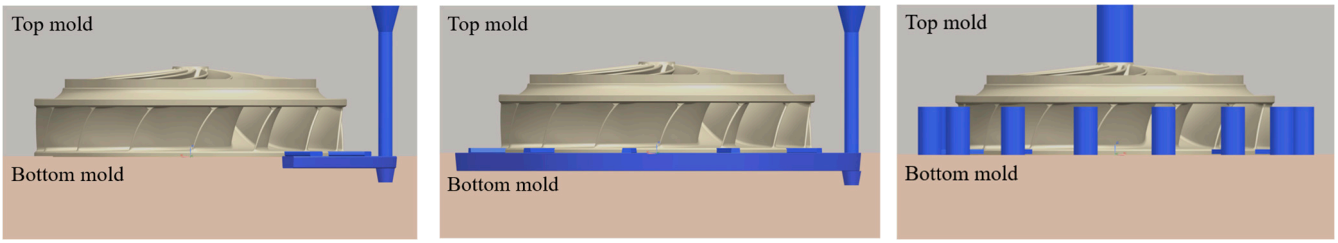

(**a**) (**b**) (**c**)

Figure 5. The division plane of mold for the backward-curved fan: (**a**) bottom-up with four gates; (**b**) bottom-up with ten gates; (**c**) top-down.

3. Method of Casting Simulation and Experiment

3.1. Casting Simulation Condition

To perform casting simulation, MAGMA V5 and the sand mold casting module were used. AlSi10Mg-Sand was selected as the alloy, and the pouring temperature into the mold was set to 720 °C. The liquidus temperature and solidus temperature are 601 °C and 549 °C, respectively. Green sand was selected as the mold material, and the initial temperature was set to 40 °C. The time for molten metal to be poured into the mold was set to 10 s. After the molten metal was completely poured into the mold, the solidification conditions were set to below solidus temperature. Sun et al. [31,32] presented an experimental result that the optimal heat transfer coefficients between aluminum alloy and the sand mold are confirmed to be 1000 to 1800 W/m^2K. The heat transfer coefficient value was set to 1800 W/m^2K between the sand mold and casting alloy and 800 W/m^2K between the top sand mold and bottom sand mold.

3.2. Experiment Condition

The material used in the casting experiment was an Al-Si-Mg aluminum alloy. In the field, it is widely known as the A360. Table 2 shows the chemical composition of A360. The main components are Si at 9.90% and Mg at 0.40%. It has excellent fluidity, and mechanical properties can be improved through heat treatment [29,33–36]. The initial temperature of the A360 alloy in the mold was 720 °C, the same as the simulation conditions. After pouring molten metal into the sand mold, it was solidified. Then, the sand mold was destroyed, and the casting was taken out.

Table 2. Chemical composition of Al-10Si-Mg alloy (weight percent).

Si	Mg	Fe	Mn	Zn	Cu	Cr	Ti	Ni	Pb	V	Al
9.90	0.40	0.30	0.30	0.20	0.20	0.04	0.03	0.03	0.02	0.01	Bal.

Tensile specimens and hardness specimens were processed from the back shroud of the manufactured fan. The standard dimension of the ASTM E8/E8M [37] Rectangular tension test specimen was used. The gage length and width are 50 mm and 12.5 mm, respectively. The thickness of the tensile specimen is 5 mm. A tensile test was performed at a strain rate of 1 mm/min, and a total of six tests were performed with the same specimen and conditions. Hardness was measured using micro Vickers hardness a total of five times. The X-ray images were taken before performing the tensile test. In the case of X-ray analysis, the entire fan could not be photographed because it was large (Ø645 mm × 180 mm). Therefore, an X-ray was taken of the tensile test specimen machined from the back shroud.

4. Results of Simulation and Experiment

4.1. Casting Simulation

Figures 6–10 show the casting simulation results of MAGMA V5 SW. Figure 6 shows a graph of the flow velocity of molten metal flowing from the gate to the fan for the bottom-up-type gating system.

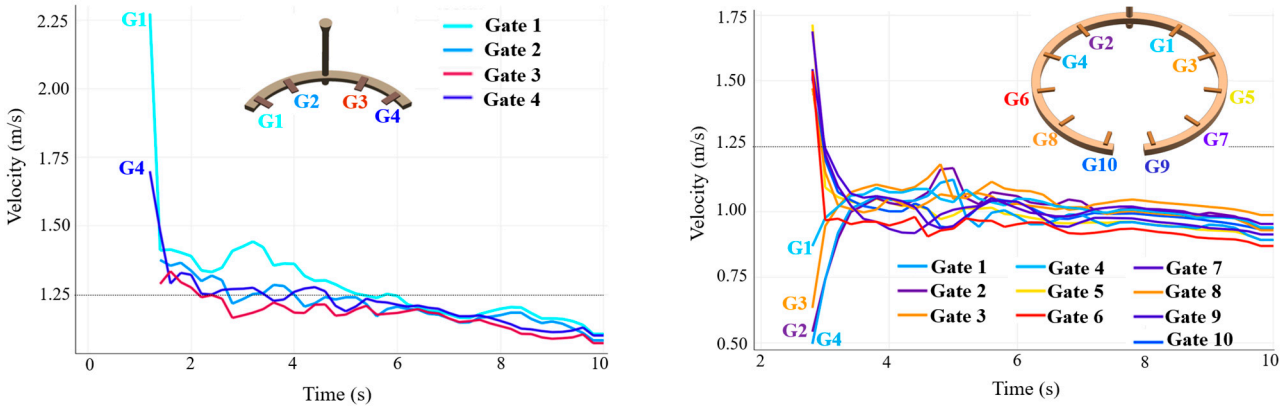

(**a**) (**b**)

Figure 6. Flow velocity of molten metal at each gate: (**a**) bottom-up type with four gates; (**b**) bottom-up type with ten gates.

Figure 6a shows a graph for the bottom-up with four gates in Figure 4a. The flow velocity of gates 1 and 4 (G1, G4) far from the sprue is higher than that of gates 2 and 3 (G2, G3) near the sprue. In particular, the initial flow velocity shows a noticeable difference. Gates 2 and 3 are approximately 1.30 m/s, and gates 1 and 4 are about 1.75 m/s. It can be determined that the first molten metal flowing into the fan comes from gates 1 and 4. Once molten metal begins to flow into the fan, the flow continues at a velocity of about 1.25 to 1.00 m/s. Figure 6b shows a graph of the bottom-up with ten gates, as shown in Figure 4b. Similar to the results in Figure 6a, the initial flow velocity of gates 5 to 10 far from the sprue is much higher than that of gates 1 to 4 near the sprue. When molten metal begins to flow into the fan, the molten metal passes through the gates at a velocity of approximately 1.00 m/s. By increasing the number of gates in the bottom-up gating system, the flow velocity flowing into the cavity can be made more stable. In the case of the top-down type, the velocity of molten metal flowing into the fan through the feeder is approximately 1.8 m/s.

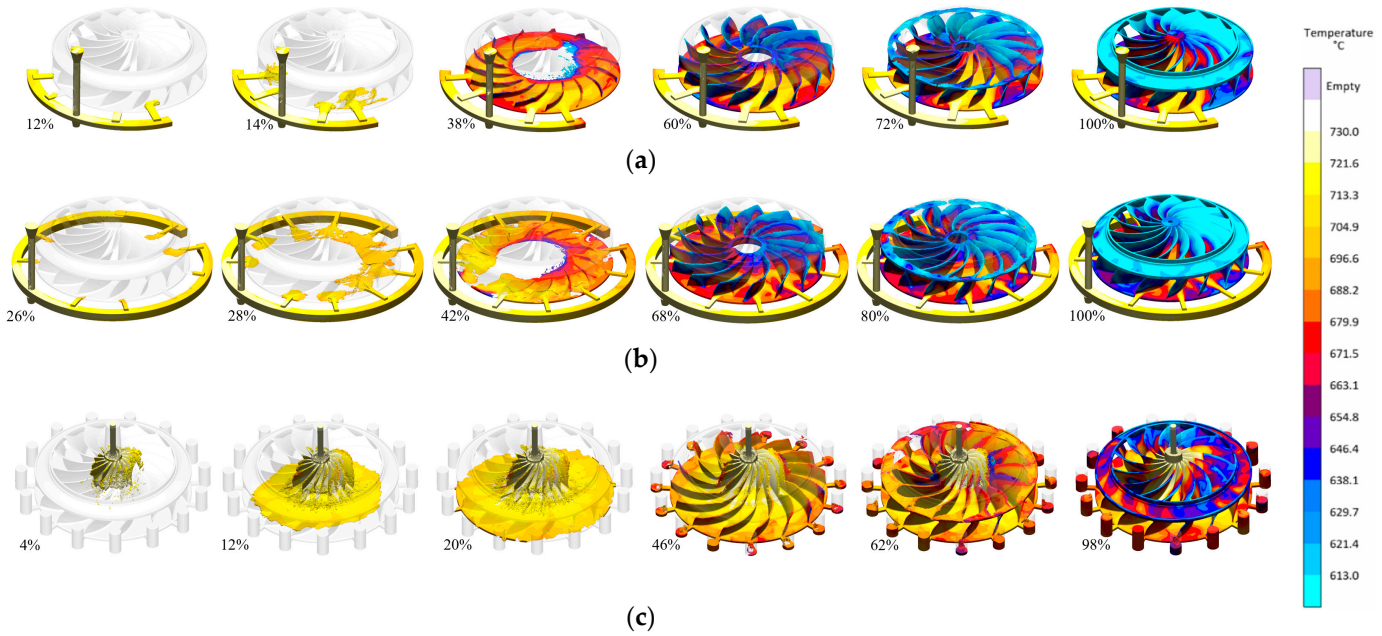

Figure 7. Temperature change distribution of molten metal in mold cavity: (**a**) bottom-up with four gates; (**b**) bottom-up with ten gates; (**c**) top-down type.

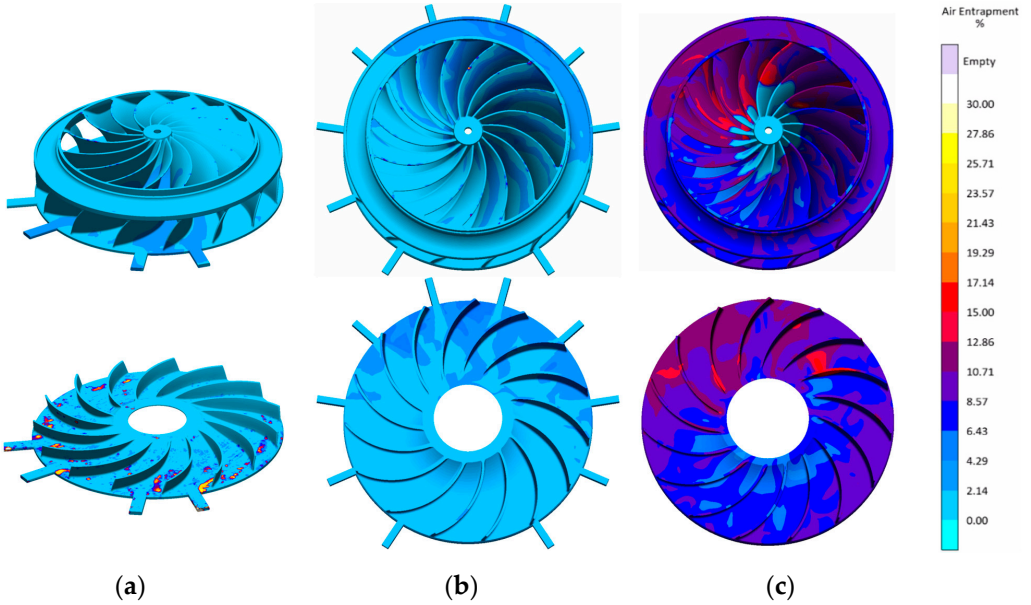

Figure 8. Air entrapment in mold cavity: (**a**) bottom-up with four gates; (**b**) bottom-up with ten gates; (**c**) top-down type.

Figure 7 shows simulation results showing the temperature change while molten metal is filled into the mold cavity. The flow pattern and temperature change of molten metal are checked, and the temperature is expressed in color. Figure 7a shows the simulation results for the bottom-up type with four gates in Figure 4a. When molten metal passes through from the sprue, it flows along the runner and arrives at the end of the runner. Molten metal begins to flow into the fan cavity from gates 3 and 4. As the molten metal passes through the gates, some splash occurs. Molten metal is filled from the bottom of the fan connected to the gate, but the area opposite the runner experiences a temperature drop. As molten metal flows into relatively thin blades, significant temperature loss occurs. It can be seen that the temperature decrease is even greater for the blades on the opposite side of the

runner. The temperature loss when 730 °C molten metal is poured into the mold and filled into the blade area is 60 to 90 °C. When the molten metal reaches the front shroud, the temperature of the molten metal is 620~613 °C, which is close to the liquidus temperature of the A360 material. When the molten metal reaches the upper part of the blades, the pouring of molten metal is completed. After pouring is completed, the temperature of the upper part of the blades and front shroud is 583 °C, which is 30 °C lower than the liquidus temperature. From the simulation results, it is determined that the upper part of the blades and front shroud are highly likely to be unfilled with molten metal.

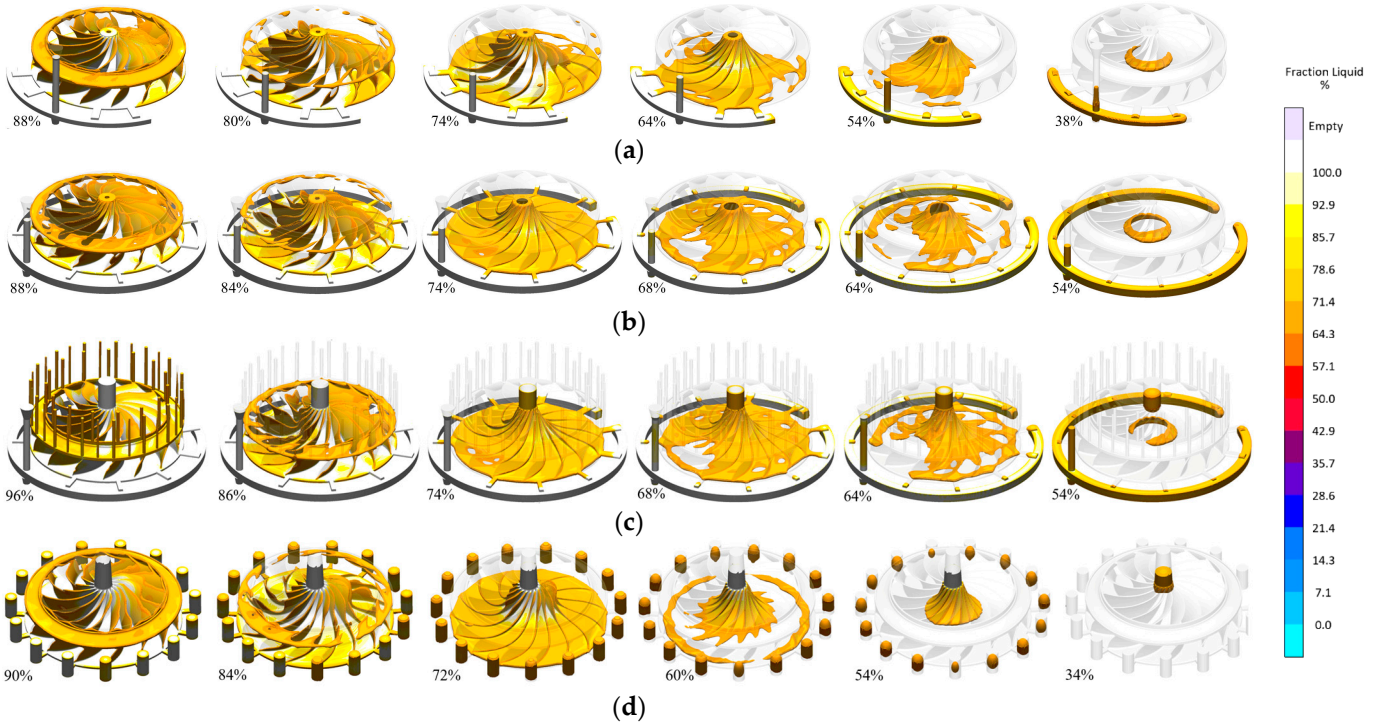

Figure 9. Solidification pattern of molten metal in mold cavity: (**a**) bottom-up with four gates; (**b**) bottom-up with ten gates; (**c**) bottom-up with ten gates and risers; (**d**) top-down type.

Figure 7b shows the simulation results for the bottom-up type with ten gates, as shown in Figure 4b. Molten metal arrives at the runner, and the molten metal begins to flow into the fan from gates 7 to 10 (farthest from the sprue). Most of the bottom of the fan is filled with molten metal through gates 7 to 10. Therefore, the pattern in which molten metal fills the bottom of the fan is not uniform. The area around the sprue is filled last. While the bottom of the fan is filled, the molten metal moving to the center splashes, and temperature loss occurs. As the blades are filled, the molten metal experiences a temperature loss of more than 60 °C. The area of temperature loss is larger in the blades on the opposite side of the sprue. The pattern of molten metal filling at the bottom of the fan is different from Figure 7a, but the pattern of filling the blades is similar. After the pouring of molten metal is completed, the temperature of the upper part of the blades and front shroud is 593 °C, which is 20 °C lower than the liquidus temperature. From the simulation results, it is judged that there is a high possibility that the upper part of the blades and front shroud are unfilled with molten metal. By increasing the number of gates in the bottom-up gating system from four to ten, the temperature loss of the molten metal filled in the mold cavity can be reduced by about 10 °C.

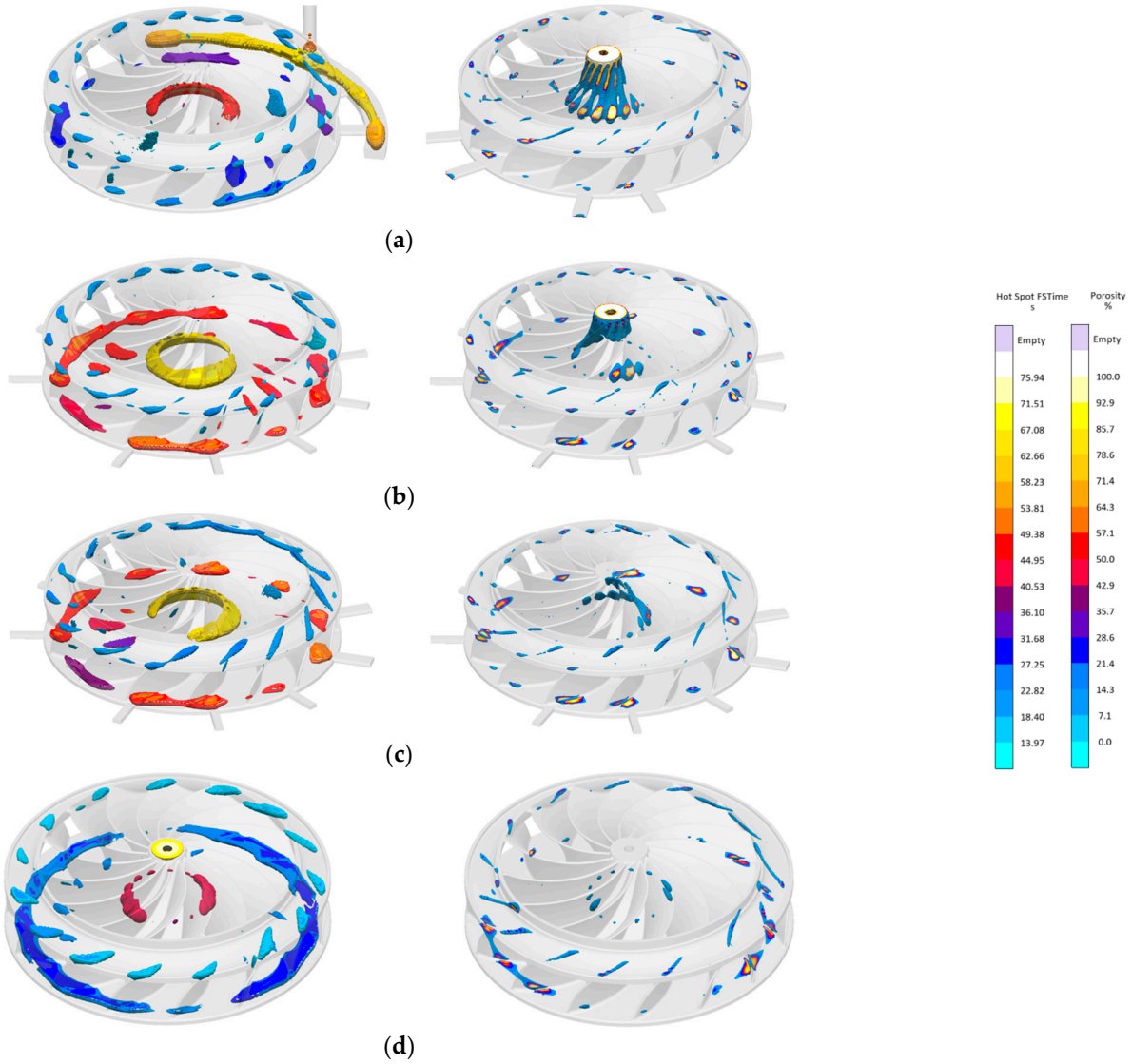

Figure 10. Distribution of hotspot and porosity after solidification: (**a**) bottom-up with four gates; (**b**) bottom-up with ten gates; (**c**) bottom-up with ten gates and risers; (**d**) top-down type.

Figure 7c shows the simulation results for the top-down type of Figure 4c. Molten metal flows directly into the fan through the feeder located in the center. Because the path of molten metal moving to the fan is short, the initial temperature of molten metal flowing into the fan is more than 10 °C higher than that of the bottom-up type. Molten metal flows into the bottom of the fan as it moves from the center to the blade's area of a radius of about 150 mm. When the lower part of the fan is filled, the molten metal rises and the blades are filled. During the process of filling the bottom of the fan with molten metal, the molten metal moving to the blades shows a turbulent flow. When molten metal arrives at the overflows, the 15 blades begin to fill almost equally. While the blades are filled with molten metal, an overall temperature loss of 40 °C to 50 °C occurs. When the molten metal arrives at the front shroud, a temperature loss of approximately 60 °C occurs only in the area where it hits the molten metal flowed into the feeder. Overall, the temperature of molten metal is above 675 °C. After the front shroud and the upper part of the blade are filled (90%), the upper part of the overflow is filled last (100%). The area with the greatest temperature loss is the upper part of the blade, and the temperature of the molten metal is over 620 °C. From the simulation results, the final temperature of the front shroud and upper part of the blade is more than 7 °C higher than the liquidus temperature. It is judged

that the possibility of molten metal being unfilled anywhere in the cavity is low. When the fan is fully filled with molten metal, about half of the overflow is filled. Therefore, if the overflow height is reduced to 50 mm, the final temperature of the molten metal flowing into the fan can be increased. The top-down type has a relatively more uniform inflow pattern of molten metal and less temperature loss than the bottom-up type.

Figure 8 shows the simulation result of the distribution of air remaining in the mold cavity after molten metal flows into the mold. Areas with an air entrapment value of 15% or more are locations where it indicates the probability of an oxide film forming, which is also considered a casting defect. The bottom-up type in Figure 8a,b shows that air is mainly collected at the bottom and blades of the fan. In the case of Figure 8a, it is considered that the possibility of porosities occurring at the bottom of the fan is quite high. Figure 8b shows that porosities are likely to occur at the top of the blades. The top-down type in Figure 8c showed air entrapment of 8 to 15% in all areas except near the hub. In the top-down, molten metal flows directly into the fan through the feeder. Even though overflows were installed, the amount of air captured in the mold cavity was greater than that of the bottom-up type. In the actual casting process, some air is removed through air vents installed in the mold. In the case of top-down, installing air vents at the top of the overflows will be effective in removing air.

Figure 9 shows how the molten metal solidifies to the solidus temperature after it flows into the mold cavity. Areas that remain liquid are expressed in color according to temperature, and areas that have solidified below the solidus temperature are expressed transparently. Regardless of the gating system type, solidification begins at the top of the fan, progresses to the bottom, and finally solidifies in the center. In Figure 9a, solidification begins first at the top of the blades located in the opposite direction of the sprue, where the temperature loss of the molten metal was large. Solidification occurs at the top of the blades and the front shroud and then at the bottom. Next, solidification occurs at the top of all blades and the front shroud, followed by solidification at the bottom. Even at the front shroud and bottom of the fan, the area opposite the sprue solidifies first. At the bottom, the border area is solidified, and then the center is solidified. Because the central thickness of the fan is thicker than the blades, solidification occurs relatively slowly. The step-by-step solidification process is a nonuniform solidification pattern in which the area opposite the sprue solidifies first, and the area near the sprue solidifies late. This is because the temperature distribution is different depending on the location when molten metal flows into the mold cavity. The solidification process in Figure 9b is similar to Figure 9a overall, but the solidification rate is more uniform at key locations (front shroud, blades, bottom). The final stage of solidification is the runner, sprue, center riser, and the upper center of the fan. Figure 9c shows the result of adding multiple risers to Figure 9b. The Ø14 mm risers are arranged at 24-degree intervals on the front shroud, and the riser of Ø70 mm is located in the center of the top of the fan. The riser of Ø70 mm in the center is the same as the feeder of the top-down type. In the fan region, the upper central part where final solidification occurs has slightly less liquid remaining than in the absence of a riser. In the case of the top-down type in Figure 9d, solidification occurs first at the top of the blades connected to the front shroud rather than at the center where the feeder is located. At the bottom of the fan, solidification occurs evenly based on the center. Unlike the bottom-up type, the location where the final solidification occurs is the central part connected to the feeder. Since the overflow inlet solidifies first before the bottom of the fan solidifies, it is necessary to increase the area of the overflow inlet to continue feeding. In the step-by-step solidification process, solidification begins at the top, progresses to the bottom, and finally progresses to the center. From the simulation results for solidification, the top-down has a better solidification pattern than the bottom-up type. And the top-down, unlike the bottom-up type, shows directional solidification.

Figure 10 shows the simulation result of hotspot and porosity (including shrinkage porosity) occurring during the solidification process. Hotspots occur where solidification is slow and are usually thick. Porosity has various causes, such as where air remains and where hot spots occur. Shrinkage porosity can occur when a liquid transforms into a solid and there is a lack of liquid feeding. This is because there may be a decrease in volume during the transformation process. In all three gating systems, hotspots mainly occur in the front shroud, back shroud, and center. The location of porosity is almost the same as that of hotspots. Blades have a relatively thin cross-sectional thickness, so hotspots do not appear, but porosity indicates the result. It can be seen that the top-down type has fewer porosity occurrence locations than the bottom-up type. As can be seen from the simulation results of the top-down, there is almost no area where pores can occur in the blades. The bottom-up type has a significant possibility of porosity occurring in the central part. In the bottom type with risers (Figure 10c), it can be confirmed that the porosity fraction in the upper central part of the fan is greatly reduced. In the top-down (Figure 10d), there is almost no possibility of porosity occurring in the center. It can be confirmed that the porosity fraction generated at the upper center of the fan is less than that of the bottom type with risers. In the case of the top-down, the amount of shrinkage that occurs during the solidification process is compensated by the feeder. It is believed that the area where porosity occurs in the back shroud will decrease if the inlet area of the overflows is increased.

4.2. Experiment

Based on the casting simulation results, the most suitable gating system for manufacturing a backward-curved fan through sand casting is the top-down type. Figure 11 shows a backward-curved fan manufactured by sand casting of A360 alloy. It can be confirmed that the molten metal was perfectly manufactured without any unfilled parts.

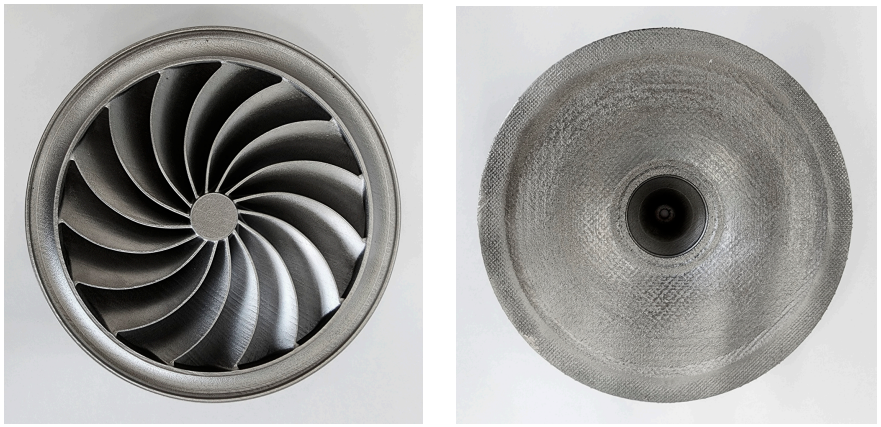

(**a**) (**b**)

Figure 11. Backward-curved fan manufactured by sand casting with top-down gating system: (**a**) front; (**b**) back.

Table 3 shows the results of the tensile test and Vickers hardness test of the manufactured backward-curved fan. Yield strength is 154.6 MPa, and tensile strength is 299.8 MPa. Elongation is 3.6%. Vickers hardness is 65 HV. Figure 12 shows an X-ray image of the tensile specimen machined from the manufactured backward-curved fan. As can be seen in the X-ray image, the appearance of porosity is not confirmed. Figure 13 shows the microstructures at the front shroud, back shroud, and blade positions of the manufactured backward-curved fan. Microstructures were measured at three locations in the front shroud, back shroud, and blade regions, respectively. The three locations were spaced 120 degrees apart in the circumferential direction. In the back shroud, the α-Al phase is more numerous

than the eutectic phase, and the α-Al phase is formed as a dendrite structure. In the front shroud and blade, the eutectic phase is more numerous than the α-Al phase, and there are also many fine α-Al phases. Since the solidification rate is different for each location, the microstructure is also considered to be different for each location. It is believed that the growth of the α-Al phase occurred in the back shroud area because the solidification process was relatively slow. The front shroud and blade are considered to have a small α-Al phase because the solidification process proceeds relatively quickly.

Table 3. Mechanical properties of the backward-curved fan manufactured by sand casting with a top-down gating system.

Yield Strength (MPa)	Tensile Strength (MPa)	Elongation (%)	Hardness (HV)
154.6 ± 6.4	299.8 ± 16.2	3.6 ± 2.6	65 ± 8

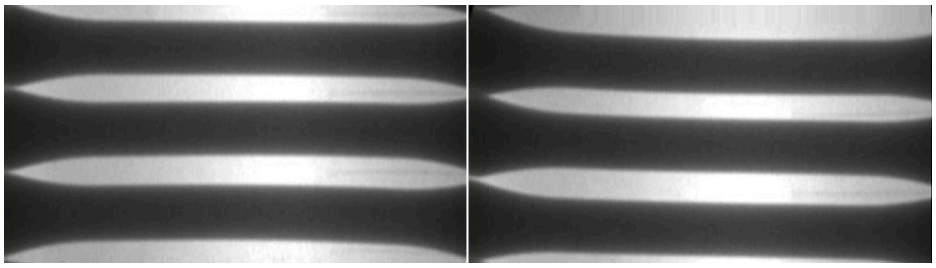

Figure 12. X-ray image of tensile specimens machined in back shroud.

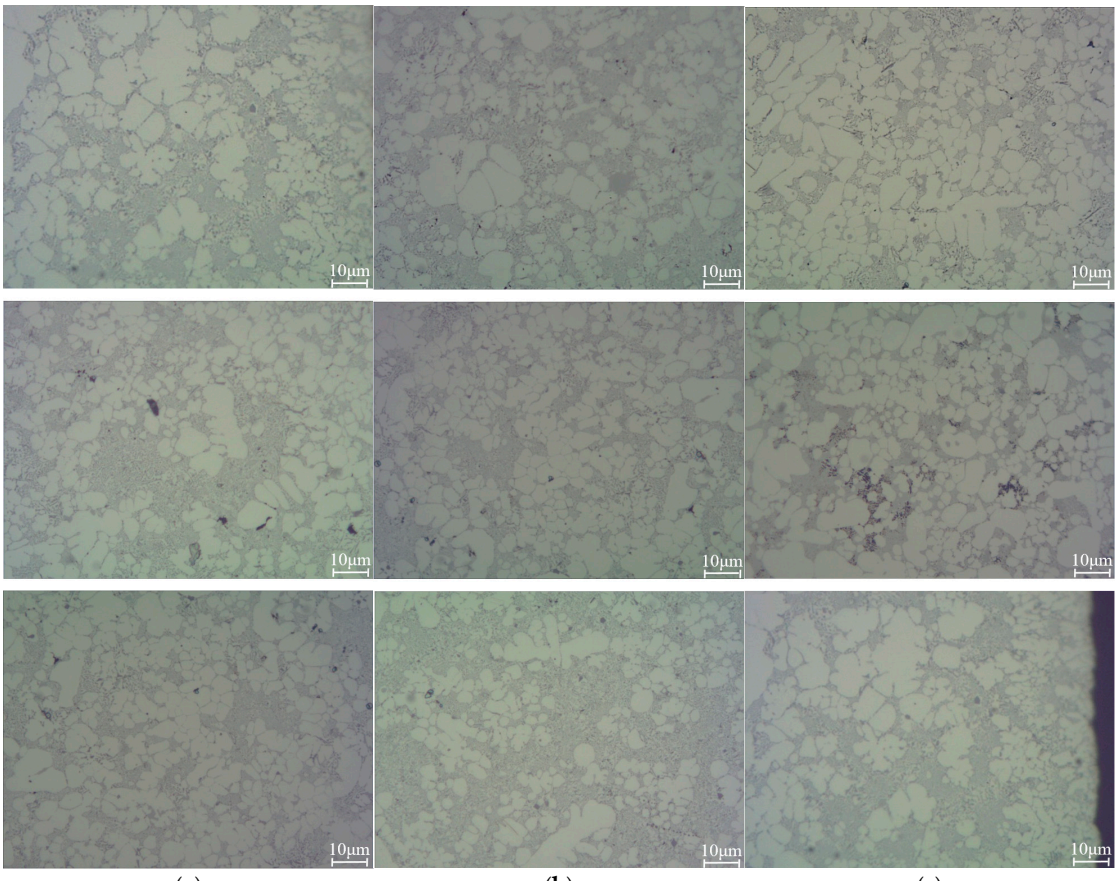

Figure 13. Microstructures of the backward-curved fan manufactured by sand casting with a top-down gating system: (**a**) front shroud; (**b**) back shroud; (**c**) blade.

5. Conclusions

In this study, a large-sized backward-curved fan with 15 blades was designed, and fan performance was roughly predicted from flow analysis. Three gating systems were designed to produce a large-sized backward-curved fan using the aluminum sand casting method. From the casting simulation results, the optimal gating system suitable for the fan shape was selected. As a result, the fan produced had soundness. The main results are as follows:

(1) Static pressure from the fan's inlet to the outlet is 8674.5 Pa. When multiplied by the rotation speed (4600 rpm), the torque acting on the fan is 286.8 N·m. The required power of 138.2 kW is calculated. When running the fan, the maximum total deformation and equivalent stress are so small that they can be ignored;

(2) In the case of the bottom-up type with four gates, a large temperature loss occurs while molten metal flows into the blades. At the top of the blades and front shroud, the temperature of the molten metal is below the liquidus temperature. When the number of gates is increased from four to ten, the flow pattern is similar. In the case of the top-down type, in which molten metal flows into the fan directly from the feeder, splashes of molten metal occur compared to the bottom-up, but the temperature loss while flowing into the blades is much smaller. After the inflow of molten metal into the mold cavity is completed, the temperature at the top of the blades and front shroud is higher than the liquidus temperature;

(3) In the bottom-up type, the solidification pattern of molten metal is not uniform, and isolated solidification occurs in some areas. Accordingly, there are many areas where hotspots and porosity are likely to occur. The top-down type showed a more uniform solidification pattern than the bottom-up. In the top-down type, directional solidification progressed due to the feeder located in the center. The feeder acted as a riser to compensate for the shrinkage of the relatively thick central part. The simulation results of hotspot and porosity were also much smaller for the top-down type than the bottom-up;

(4) From the casting simulation results, the gating system suitable for the backward-curved fan is the top-down type. The manufactured fan had soundness without any unfilled parts.

Funding: This work was supported by the Kyungnam University Foundation Grant, 2023.

Data Availability Statement: The original contributions presented in this study are included in the article. Further inquiries can be directed to the corresponding author.

Conflicts of Interest: The author declares no conflicts of interest.

References

1. Son, K.J. Thermo-Electro-Fluidic Simulation Study of Impact of Blower Motor Heat on Performance of Peltier Cooler for Protective Clothing. *Energies* **2023**, *16*, 4052. [CrossRef]
2. Zinchenko, A.; Baiul, K.; Krot, P.; Khudyakov, A.; Vashchenko, S.; Banasiewicz, A.; Wróblewski, A. Materials Selection and Design Options Analysis for a Centrifugal Fan Impeller in a Horizontal Conveyor Dryer. *Materials* **2021**, *14*, 6696. [CrossRef]
3. Le, T.L.; Nghia, T.T.; Thong, H.D.; Son, M.H.K. Numerical study of aerodynamic performance and flow characteristics of a centrifugal blower. *Int. J. Intell. Unmanned Syst.* **2023**, *11*, 396–406. [CrossRef]
4. Lee, Y.T.; Lim, H.C. Performance assessment of various fans ribs inside a centrifugal blower. *Energy* **2016**, *94*, 609–622. [CrossRef]
5. Amer, M. A novel bionic impeller for laptop cooling fan system. *Results Eng.* **2023**, *20*, 101558. [CrossRef]
6. Hsu, Y.S.; Zheng, X.; Cooper, E.; Gillott, M.; Wood, C.J. Evaluation of the indoor pressure distribution during building airtightness tests using the pulse and blower door methods. *Build. Environ.* **2021**, *195*, 107742. [CrossRef]
7. Cattanei, A.; Zecchin, F.M.; Pasquali, A.D.; PhD, A.L. Effect of the uneven blade spacing on the noise annoyance of axial-flow fans and side channel blowers. *Appl. Acoust.* **2021**, *177*, 107924. [CrossRef]

8. Jerchel, M. Leopard 2 Main Battle Tank 1979–1998. *New Vanguard* **1998**, *1*, 1–48.
9. Aigboje, E.O.; Odiamenhi, A.M. Design and Fabrication of Centrifugal Blower using Locally Sourced Materials. *J. Electr. Control Technol. Res.* **2021**, *3*, 11–19. [CrossRef]
10. Draghici, S.; Vintila, I.S.; Mihalache, R.; Petrescu, H.A.; Tuta, C.S.; Hadar, A. Design and Fabrication of Thermoplastic Moulds for Manufacturing CFRP Composite Impeller Blades. *Mater. Plast.* **2020**, *57*, 290–298. [CrossRef]
11. Aung, K.; Sein, N.W.; Nyi, N. Design and Fabrication of impeller for Single Suction Centrifugal Pump. *Int. J. Sci. Res. Publ.* **2019**, *9*, 799–805. [CrossRef]
12. Hernández, F.; Fragoso, A. Fabrication of a Stainless-Steel Pump Impeller by Integrated 3D Sand Printing and Casting: Mechanical Characterization and Performance Study in a Chemical Plant. *Appl. Sci.* **2022**, *12*, 3539. [CrossRef]
13. Kim, J.T.; Kim, S.I.; Choi, J.Y.; Koo, C.W. A 3D Miniaturized Glass Magnetic-Active Centrifugal Micropump Fabricated by SLE Process and Laser Welding. *Micromachines* **2022**, *13*, 1331. [CrossRef] [PubMed]
14. Iqbal, H.; Sheikh, A.K.; Al-Yousef, A.H.; Younas, M. Mold Design Optimization for Sand Casting of Complex Geometries Using Advance Simulation Tools. *Mater. Manuf. Process* **2012**, *27*, 775–785. [CrossRef]
15. Kim, E.H.; Choi, H.H.; Jung, Y.G. Fabrication of a ceramic core for an impeller blade using a 3D printing technique and inorganic binder. *J. Manuf. Process* **2020**, *53*, 43–47. [CrossRef]
16. Pratesa, Y.; Munir, B.; Najamuddin, S. Application of Casting Simulation in Failure Analysis of Impeller. *J. Fail. Anal. Prev.* **2019**, *19*, 431–437. [CrossRef]
17. Anggono, A.D.; Prihtiantoro, D.; Siswanto, W.A. Casting Design, Simulation and Manufacturing Validation of Air Compressor Fan Blade. *Int. J. Mech. Mechatron. Eng.* **2020**, *20*, 181–189.
18. Khan, M.A.A.; Sheikh, A.K.; Asad, M. Mold Design and Casting of an Impeller Using MAGMASoft. *Int. J. Mech. Eng. Robot. Res.* **2020**, *9*, 1579–1583. [CrossRef]
19. CHEN, L.; LING, Y.; KANG, X.; XIA, L.; LI, K. Numerical Simulation of Stress and Deformation for a Duplex Stainless Steel Impeller during Casting and Heat Treatment Processes. *J. Mater. Sci. Technol.* **2008**, *24*, 364–368.
20. Dermawan, A.; Pramono, A.E. Engineering and Process of Investment Casting for Pump Impellers. *RiESTech* **2023**, *1*, 11–19.
21. Wang, D.; Dong, A.; Zhu, G.; Shu, D.; Sun, J.; Li, F.; Sun, B. Rapid casting of complex impeller based on 3D printing wax pattern and simulation optimization. *Int. J. Adv. Manuf. Technol.* **2016**, *100*, 2629–2635. [CrossRef]
22. Choe, C.M.; Yang, W.C.; Kim, U.K.; Ri, B.G.; Om, M.S. Manufacture of centrifugal compressor impeller using FDM and investment casting. *Int. J. Adv. Manuf. Technol.* **2022**, *118*, 173–181. [CrossRef]
23. Kuo, J.K.; Huang, P.H.; Lai, H.Y.; Chen, J.R. Optimal gating system design for investment casting of 17-4PH stainless steel enclosed impeller by numerical simulation and experimental verification. *Int. J. Adv. Manuf. Technol.* **2017**, *92*, 1093–1103. [CrossRef]
24. Wang, D.; Sun, J.; Dong, A.; Shu, D.; Zhu, G.; Sun, B. An optimization method of gating system for impeller by RSM and simulation in investment casting. *Int. J. Adv. Manuf. Technol.* **2018**, *98*, 3105–3114. [CrossRef]
25. MA, X.; Zhuang, Y.; Tao, Y. Numerical Simulation of Die-casting Magnesium Alloy Impeller with the Central Gating System. *Appl. Mech. Mater.* **2011**, *55–57*, 2126–2129.
26. Liu, Y.; He, H.; Gao, J.; Li, G.; Liang, Y.; Li, L. Research on the low-pressure casting process of a double suction impeller in 304 austenitic stainless steel with high performance and thin-wall complex structure. *J. Phys. Conf. Ser.* **2022**, *2390*, 012078. [CrossRef]
27. Wallace, G.; Jackson, A.P.; Midson, S.P.; Zhu, Q. High-quality aluminum turbocharger impellers produced by thixocasting. *Trans. Nonferrous Met. Soc.* **2010**, *20*, 1786–1791. [CrossRef]
28. Hafeez, F.; Ahmed, N.; Ali, M.A.; Farooq, M.U.; Rehman, A.U. A comprehensive efficiency evaluation of conventional and ablation sand casting on the example of the AlSi7Mg alloy impeller. *Int. J. Adv. Manuf. Technol.* **2022**, *121*, 3653–3672. [CrossRef]
29. Caceres, C.H.; Davidson, C.J.; Griffiths, J.R.; Wang, Q.G. The Effect of Mg on the Microstructure and Mechanical Behavior of Al-Si-Mg Casting Alloys. *Metall. Mater. Trans.* **1999**, *30*, 2611–2618. [CrossRef]
30. Seo, H.Y.; Jin, C.K.; Kang, C.G. Design of a gate system and riser optimization for turbine housing and the experimentation and simulation of a sand casting process. *Adv. Mech. Eng.* **2018**, *10*, 1–12. [CrossRef]
31. Sun, J.J.; Le, Q.C.; Wang, T.; Zhao, X.; Shi, W.S.; Huo, H.W.; Wang, C. Investigation on heat-transfer-coefficient between aluminum alloy and organic inorganic sand mold based on inverse method. *Res. Dev.* **2019**, *16*, 336–341. [CrossRef]
32. Yang, H.; Shan, Z.; Wang, Y.; Liu, L. Simulation of temperature field of A356 aluminum alloy in freeze casting. *J. Phys. Conf. Ser.* **2020**, *1600*, 012045. [CrossRef]
33. Wang, Q.G.; Davidson, C.J. Solidification and precipitation behaviour of Al-Si-Mg casting alloys. *J. Mater. Sci.* **2001**, *36*, 739–750. [CrossRef]
34. Shabestari, S.G.; Moemeni, H. Effect of copper and solidification conditions on the microstructure and mechanical properties of Al-Si-Mg alloys. *J. Mater. Process. Technol.* **2004**, *153–154*, 193–198. [CrossRef]
35. Wang, Y.; Liao, H.; Wu, Y.; Yang, J. Effect of Si content on microstructure and mechanical properties of Al-Si-Mg alloys. *Mater. Des.* **2014**, *53*, 634–638. [CrossRef]

36. Cheng, W.; Liu, C.Y.; Huang, H.F.; Zhang, L.; Zhang, B.; Shi, L. High strength and ductility of Al-Si-Mg alloys fabricated by deformation and heat treatment. *Mater. Charact.* **2021**, *178*, 111278. [CrossRef]
37. *ASTM E8*; Standard Test Methods of Tension Testing of Metallic Materials. American Society for Testing and Materials: Montgomery, PA, USA, 2024; Volume 3.01.

Disclaimer/Publisher's Note: The statements, opinions and data contained in all publications are solely those of the individual author(s) and contributor(s) and not of MDPI and/or the editor(s). MDPI and/or the editor(s) disclaim responsibility for any injury to people or property resulting from any ideas, methods, instructions or products referred to in the content.